Scientific Reports

https://doi.org/10.1038/s41598-025-33950-3

Article in Press

Ultra-sensitive graphene–gold hybrid dual core photonic crystal fiber sensor based on surface plasmon resonance for bio-analyte detection

Received: 18 October 2025

Accepted: 23 December 2025

Published online: 12 February 2026

Cite this article as: Maurya V.C., Trabelsi Y., Varshney A.D. *et al.* Ultra-sensitive graphene–gold hybrid dual core photonic crystal fiber sensor based on surface plasmon resonance for bio-analyte detection. *Sci Rep* (2025). https://doi.org/10.1038/s41598-025-33950-3

Vikas Chandra Maurya, Youssef Trabelsi, Anshu D Varshney & Suneet Kumar Awasthi

Ultra-Sensitive Graphene–Gold Hybrid Dual Core Photonic Crystal Fiber Sensor Based on Surface Plasmon Resonance for Bio-Analyte Detection

Vikas Chandra Maurya[1], **Youssef Trabelsi**[2], **Anshu D Varshney**[1], **and Suneet Kumar Awasthi**[1,*]

[1]Department of Physics and Material Science and Engineering, Jaypee Institute of Information Technology, Noida 201304, U.P., India
[2]Applied College at Mahail Aseer, Physics Department, King Khalid University, Abha, Saudi Arabia
[*]Corresponding author email- suneet_electronic@yahoo.com

ABSTRACT

This research work deals with highly sensitive detection capabilities of dual core photonic crystal fiber(PhCF) biosensor. It works on the principal of surface plasmon resonance (SPR) and consisted of hybrid coatings of graphene and gold layers for efficient detection of low refractive index (RI) values ranging from 1.30 to 1.39 in steps of 0.01 of bio-analytes. This design is integration of the superior plasmonic properties of gold with an exceptionally high absorptive and conductivity properties of graphene for improving the light–matter interaction, in addition to signal stability. The thicknesses of hybrid layer consisted of gold and graphene layers are optimized to make our design highly sensitive by using numerical simulations carried out in COMSOL Multiphysics 6.0 and MATLAB softwares. It yields thicknesses of gold and graphene layers to 40 nm and 9.52 nm respectively. The proposed design loaded separately with range of analytes of low refractive indices from 1.30 to 1.39 exhibiting an outstanding wavelength dependent sensitivity and resolution values of 30,000 nm/RIU and 3.33×10^{-6} RIU, respectively apart from other promising values of various parameters. These results show that the proposed design possesses a significant improvement in performance over the existing counterparts. The proposed design points out the excellent sensing feature for precise, immediate and reliable detection of disease diagnostics and other biomedical sensing applications.

Keywords: Dual-core photonic crystal fiber, Graphene enhanced SPR sensor, Plasmonic biosensing, Wavelength sensitivity, Biomedical diagnostics

Introduction

Electromagnetic wave (EMW) propagation through the period structure was first studied by Lord Rayleigh in 1857. These structures are formed by periodically varying dielectric constants or refractive indices (RIs) of the constituent materials and are known as photonic crystals (PhCs) as pioneered by Yablonovitch and John in 1987. This periodic variation of RIs of constituent materials is responsible for the formation of a photonic band gap (PhBG), similar to the electronic band gap found in semiconductors. The beauty of the PhBG is to command and control the propagation of EMWs passing through PhCs in a better way. It results the design and development of modern photonic devices that are used in the field of defense, biomedical sciences, chemical and communication industries etc. Based on the periodicity of the constituent materials, PhCs are articulated as one- (1), two-(2) and three-(3) dimensional (D) photonic structures. PhCs have revolutionized the fabrication of advanced optical devices useful in the field of plasmonics and photonics. Photonic devices are technologically capable of addressing the challenges faced during their realization due to excellent command and better control over the propagation of light passing through them[1]. Owing to their resemblance to semiconductors which possess an electronic bandgap, PhCs are often referred as "semiconductors of photons." They can be fabricated from a wide range of materials, offering excellent flexibility and compatibility with different material systems[2].

Conventional optical fibers used in communication and optical sensing applications are unable to provide design flexibility in the development of advanced photonic devices. However, photonic crystal fiber (PhCF) based devices are capable of addressing these limitations significantly. PhCFs are a distinct category of optical fibers characterized by a microstructured arrangement, where a high refractive index region is surrounded by low refractive index material[3]. Photonic devices made up of PhCFs provide flexibility of modifying the geometrical structures. Generally, background material of most of the PhCFs is silica. PhCFs consist of air hole along its length which, helps in confinement of light and guide it effectively. The propagation of

light inside PhCF is governed by law of total internal reflection similar to conventional fibers[4]. Its core can be hollow or solid, depending upon its application. The core is encompassed via air-holes named as as micro structured (holey) fiber[4]. PhCFs are generally classified in two categories - (1) Index-Guiding (IG) and (2) PhBG. It it essential that RI value of fiber core should be larger than the effective index of refraction (ERI) of fiber cladding to guide the light into fiber core.

In recent years, optical sensing technology (OST) has attracted significant research attention because of its diversified applications in various fields like medical diagnostics, environmental preservation, and chemical analysis. Amongst various sensing approaches, photonic crystal fiber based sensors employing SPR, are emerged as one of the most advanced and efficient techniques. SPR based studies on sensors emerged extensively over the past two decades due to remarkably high sensitivity, real-time tracking of molecular interactions, and pinpoint accuracy. The interaction of light with surface plasmon waves (SPWs) results SPR phenomena at the interface between metal and dielectric. Depending on the coupling mechanism, the three important configurations resulting SPR are prism-, grating- and waveguide-coupled mechanism.[5]. Amongst the available SPR coupling methods, prism-based configurations—specifically the Otto and Kretschmann configurations—are the most widely used. The Otto configuration requires a hollow gap for SPR excitation created between the prism and thin layer of metal. Its coupling efficiency is poor so limits practical use. In contrast, the Kretschmann configuration is more effective and has become the most popular choice in OST due to its enhanced sensing performance. However, prism-based SPR sensors are generally bulky and often require moving mechanical accessories, which limits their suitability for compact setups or remote sensing applications.[6].

SPR sensors built on optical fiber platform have successfully addressed many of the disadvantages of traditional prism-coupled mechanism. The performance of such SPR based optical fiber sensors (OFSs) is examined experimentally as well as theoretically. In 1993, Sir R. C. Jorgenson demonstrated first SPR sensor fabricated on optical fiber (OF) platform by removing a section of OF cladding. After cleaning it is polished by thin layer of gold to excite surface plasmons (SPs)[7]. However, conventional fiber-optic SPR sensors offer limited design flexibility and operate with a relatively small acceptance angle[6]. To overcome these drawbacks, PhCFs have been extensively studied due to their structural flexibility and enhanced light–matter interaction. Depending on the application, PhCFs allow precise control over propagation of leaky-core-guided-mode by tailoring the geometries of structure like hexagonal, square, octagonal, decagonal, or hybrid lattice designs—and by optimizing critical parameters of the fiber structure like air-hole diameter, pitch, and overall lattice configuration[8–10]. Moreover, the penetration of light propagating via core-cladding regions of SPR based PhCF strucure reaches to metallic region and generates evanescent field. Its interaction with free electrons available at metal-dielectric interface excites surface plasmon waves (SPWs) propagating parallel to the interface. When the frequency of oscillation of free electrons on the surface of gold becomes equal to the frequency of oscillation of incident photon, a sharp resonance peak occurs because of strong resonance[11]. At this resonance condition, the propagation loss reaches to its maximum for given RI value of analyte. The existence of this peak is due to the result of SPR. By analyzing the shift in position and intensity of the loss peak the tiny change in the RI value of analyte can easily be obtained.

The selection of plasmonic layer of metal in any PhCF-based SPR sensors, is always crucial designing aspect because it determines the performance of the sensor. Commonly used plasmonic metals in any SPR sensor are gold, aluminum, silver and copper[6,11–15]. Each of these metals exhibits unique properties as well as certain limitations when employed as plasmonic layers. For instance, silver offers low damping loss and no inter-band transition, which make it highly suitable for strong plasmonic excitation[16]. However, its tendency to oxidize in aqueous environments reduces sensing accuracy and restricts its broader application. Similarly, aluminum, with its high electron density[17], has shown potential to be used as plasmonic metal, it also suffers from oxidation issues. Besides this, gold due to its chemical stability and resistance to oxidation is alternatively adopted for designing of reliable and long-term performing SPR based biosensor[18].

A wide range of PhCF-based SPR sensor designs having improved sensing characteristics such as sensitivity and resolution have been improved by the various researchers over the past decades[19–21]. In these sensors, the plasmonic metal layer can be integrated either internally or externally. Capabilities of internal metal coated SPR sensor design infiltrated with selective liquid under investigation is demonstrated in several studies[19,22]. In this approach, some of the targeted air holes of fiber are prepared by coating them with a thin plasmonic metal. Further these air holed are loaded with analyte. However, its practical implementation is challenging due to the small dimensions of the air holes and the difficulty in controlling uniform metal deposition. In comparison, external metal coating is more feasible and has become a preferred strategy. To overcome the limitations of internal coating, various external-coated PhCF sensors have been developed, including D-shaped PhCF sensors[21,23–25], copper- and graphene-assisted PhCF SPR sensors[12,13,26,27], and other improved external structures[28,29]. D-shaped PhCF sensors, in particular, exhibit high sensitivity; however, their fabrication requires precise surface polishing, which is challenging as it demands accurate removal of a predefined region of the PhCF[20].

Besides this the dual-core fiber structure supports the symmetric and anti-symmetric super-modes to improve resonance shift and confinement loss responsible for pushing more optical energy towards the plasmonic interface where it overlaps with SPP mode. It makes phase matching conditions highly sensitive depending upon changes in RI of analyte. These RI variations

allow the super-modes to experience stronger perturbations in effective refractive index (ERI) resulting a prominent shift peak wavelength. The role of the graphene layer is to further amplify this effect by modifying the localized electric field through its surface conductivity. It improves plasmon excitation and electric field confinement at the metal–analyte interface. Consequently, at resonance more energy is coupled with SPP mode, resulting sharper confinement-loss peaks to boost sensitivity of the sensor.

Recently, SPR based externally coated PhCF sensors have attracted considerable response due to it's simple, straightforward and easy to implement architecture along with an excellent sensing performance and flexible fabrication possibilities. For instance, A. Rifat et al. suggested a hybrid PhCF biosensor consisted of graphene coated copper layer. This design achieves highest wavelength sensitivity (WS) of 2000 nm/RIU and resolution of 5.00×10^{-5} RIU in the 1.33–1.37 analyte RI range[12]. Similarly, a gold-coated PhCF SPR sensor demonstrated even higher performance, with wavelength sensitivity up to 4000 nm/RIU and sensor resolution of 2.5×10^{-5} RIU in the same analyte RI range[26]. A variety of high-performance PhCF-based SPR sensors have been reported with remarkable sensitivity and resolution. For example, a D-shaped PhCF sensor operating in the analyte RI range of 1.33–1.38 achieved a maximum wavelength sensitivity of 10,493 nm/RIU with a wavelength resolution of 9.53×10^{-6} RIU[30]. In another study, a PhCF SPR sensor incorporating niobium and aluminum oxide layers demonstrated a wavelength sensitivity of 8000 nm/RIU and a resolution of 1.25×10^{-5} RIU in the analyte range of 1.36–1.40[31]. A spiral PhCF SPR sensor employing gold as the plasmonic layer demonstrated WS value of 4300 nm/RIU with resolution of 2.17×10^{-5} RIU in the analyte RI range of 1.33–1.38[20]. Furthermore, a hexagonal lattice consisted of gold coated PhCF with two cores, exhibited outstanding sensing performance with maximum WS value of 16,000 nm/RIU and wavelength dependent resolution of 6.25×10^{-6} RIU under RI range of analytes from 1.33–1.40[6].

Motivated by above mentioned excellent piece of research work based on PhCF, We have modified the structure of Ahmed et. al [6] by incorporating a protective layer of graphene over gold layer. The results of our modified structure clearly indicate that integration of graphene remarkably improves plasmon–photon coupling to reduce damping, and enhances the interaction of evanescent fields at the sensing interface of the structure. Quantitatively, the graphene -gold hybrid design achieves highest shift in the wavelength of resonance to 300 nm for the RI variation of the sample from 1.38 to 1.39, which achieves wavelength dependent sensitivity value of 30,000 nm/RIU, whereas the gold-only design reported in reference (6) exhibits only a 160 nm shift yielding a highest WS of 16,000 nm/RIU under same RI variation from 1.39 to 1.40. But for true comparison between these two models, one should consider highest WS value of 8000 nm/RIU reported in reference (6) under the influence of the RI index variation of sample from 1.38 to 1.39 similar to the proposed work. Additionally, it should be noted that the design of Ahmed et al in reference (6) is capable to sensing samples of RI variation from 1.33 – 1.40 whereas our design is capable of sensing the samples of RI variations from 1.30 to 1.39. This actual comparison yields that our idea of including an additional proactive layer of graphene over gold in the structure reported in reference 6 is capable of drastically enhancing the maximum WS from 8000 nm/RIU to 30000 nm/RIU subjected to the RI variation of the sample from 1.38 to 1.39. The reason of this improvement is based on the fact that the graphene enhances molecular adsorption through $\pi-\pi$ stacking interactions and simultaneously prevents diffusion of the gold layer into the substrate, thereby improving both stability and durability of the sensor. Moreover, its inclusion makes the proposed hybrid sensor more sensitive towards determining any minute change in the RI of an analyte. These improvements are consistent with the observed spectral characteristics reported in the proposed work. Besides this the gold only structure in reference (6) yields high confinement loss responsible for higher signal loss, lower values of signal-to-noise ratio and making it more inconvenient for accurate detection and quantifying the small changes in the analyte like blood serum.

Nowadays, blood investigation is becoming an important and challenging diagnostic tool for identification of hematological disordering. This disordering is closely linked with range of non chronic disease like diabetes mellitus (DM), coronary artery disease, various cancers, and respiratory issues[32]. Presently, breast and prostate cancers are the two most prevalent types of cancers in the Western world. These specific cancers are accounting nearly 30% of over all cancer cases[33]. Health issues are not confined to any single nation; rather, they represent a global challenge. Therefore, blood analysis remains one of the most cost-effective, necessary, and convenient approaches for routine health monitoring[34]. The refractive indices of many clinically important fluid like human serum, urine, saliva, plasma and diluted blood components exhibit stimulated range of RIs from 1.30 to 1.39. This range of RIs makes our SPR based PhCF sensor can be use full for in the analysis of suitable for biomedical diagnostics. This range of RI window includes biomarkers like glucose and urea associated with diabetes, renal dysfunction, liver abnormalities, and early-stage cancer screening, where a minute change in RI may easily correlate with respective change in molecular concentration. By leveraging the ultrahigh WS, the proposed PhCF sensor can be used for sensing of relevant biomolecular interactions occurring at the interface of graphene and gold layers. It also opens the gateway of precise monitoring of diseases comes under the range of analyte whose refractive index variations are from 1.30 to 1.39 due to early-stage pathological changes, and low-concentration biomarker shifts. These capabilities are enough for lab-on-fiber based biosensing applications, point-of-care diagnostics, and swift screening of clinically relevant biological analytes.

In recent years, graphene assisted SPR sensors conventional Kretschmann configuration sensors have been extensively studied[35–37]. Alternatively, PhCF based SPR sensors utilizing gold or silver in combination with graphene have also worked

out to overcome the complications involved in Kretschmann geometry. In the proposed design the choice of selecting gold over the other plasmonic materials is due to its chemical stability and ability to produce larger resonance wavelength shifts compared to silver, which enhances the sensor's sensitivity[13]. Furthermore, external coatings of gold and graphene over cladding streamlines the fabrication process and enables the sample to be applied directly onto the sensor's outer surface. In such structures it is essential to analyze the mode profiles at resonance because it reveals the information about the distinct coupling pathways originating different spectral dips. Prior works already demonstrate that the electric and magnetic field distributions helps in examining the role of separate modal interactions in creating the individual resonance modes [38–45]. For instance, field-distribution analysis has been widely used to differentiate localized surface plasmon modes, cavity-induced resonances, and multi-channel coupling effects in complex plasmonic structures. By examining the spatial field patterns at each peak in the proposed sensor, one can directly confirm whether each resonance corresponds to a different super-mode–SPP coupling event rather than a numerical artifact. This approach provides strong physical justification to study the multi-peak behaviour and also strengthens the interpretation of the sensing mechanism. This work deals with a numerical investigation of a dual-core SPR-based PhCF sensor for low RI detection. The proposed sensor employs a gold plasmonic layer integrated with a thin graphene coating to analyze bio-analyte interactions within the RI range of 1.30–1.39. In this configuration, gold acts as the primary plasmonic material deposited on the PhCF structure, while graphene serves as an additional functional layer. The incorporation of graphene enhances molecular adsorption through π–π stacking interactions[35] and simultaneously prevents diffusion of the gold layer into the substrate, thereby improving both stability and durability of the sensor[46]. Our work highlights how the proposed modified design can achieve highest value of WS and wavelength dependent resolution value of 30000 nm/RIU and 3.33 $\times 10^{-6}$, respectively. Graphene does serve as a protective barrier that prevents gold oxidation and maintains long-term stability, but this is not its main contribution to the sensor for enhancing its performance. Its dominant effect comes from modifying the electric field at the interface, which cannot be achieved by protection alone.

Sensor Design Description and Methodology

The schematic diagram showing 2D cross-sectional view of the proposed SPR-based PhCF sensor is presented in Fig. 1. It is subdivided in two parts. The capillary stacking in x-y plane is depicted in Fig. 1(a), while the cross-sectional layout of the proposed SPR-based sensor is illustrated in Fig. 1(b). The central part consisted of green colour background region showing the fused silica core having fifteen air holes of different diameters as d_1, d_2, d_3 and d_4. This central part is further surrounded by four concentric cylindrical layers of materials gold, graphene, analyte and PML, shown by colours yellow, cyan, magenta and teal, respectively. Gold is preferred over silver as the plasmonic medium due to its superior chemical and environmental stability compared to silver. The nano interface of graphene established between gold and the analyte provides an enhanced coupling. The parameters of optimized geometry of the design are: diameter of the air-hole located at centre $d_1 = 0.882, \mu$m, the diameter of air-holes forming inner ring around central air hole $d_2 = 0.504, \mu$m, and diameters of air-holes forming outer ring $d_3 = 1.620, \mu$m and $d_4 = 1.746, \mu$m. The lattice period, which is the spacing between centers of adjacent air-holes of the outer air-hole ring, is $\Lambda = 1.8, \mu$m. The optimum thicknesses of cylindrical layers of materials gold and graphene are $t_{gold} = 40$ nm $t_{gr} = 9.52$ nm, respectively. The coatings of gold and graphene can be realized by using either electron-beam evaporation or sputtering thin film deposition techniques[47,48].

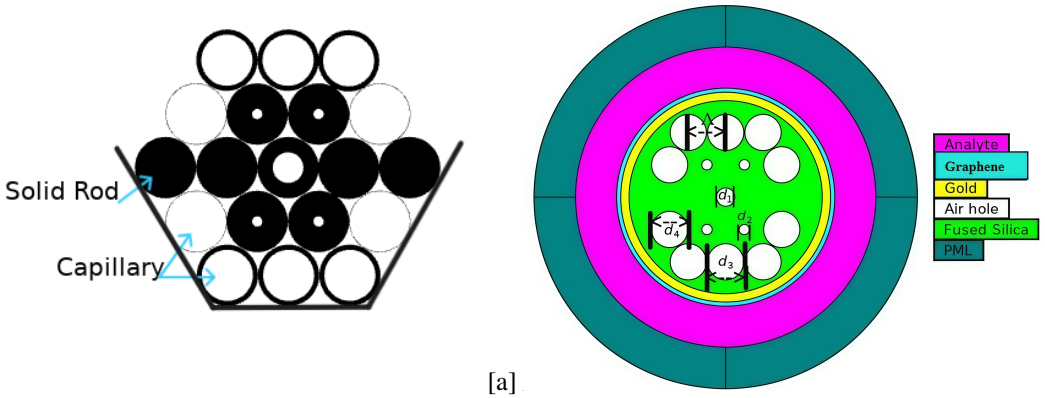

[a] [b]

Figure 1. Deception of our bio sensing PhCF design (a) capillary stacking view shown in x-y plane, and (b) 2D cross-sectional view.

The wavelength dependent RI values of fused silica can be calculated by following Sellmeier equation (1) as[6]

$$n^2(\lambda) = 1 + \frac{b_1\lambda^2}{\lambda^2 - c_1^2} + \frac{b_2\lambda^2}{\lambda^2 - c_2^2} + \frac{b_3\lambda^2}{\lambda^2 - c_3^2} \tag{1}$$

where, $b_1 = 0.69616300$, $b_2 = 0.407942600$, $b_3 = 97.9340025$ and ${c_1}^2 = 4.67914826 \times 10^{-3}\mu m^2$, ${c_2}^2 = 1.35120631 \times 10^{-3}\mu m^2$, ${c_3}^2 = 97.9340025 \times 10^{-3}\mu m^2$ are the Sellmeier coefficients. Here symbol λ is representing incident wavelength measured in micrometer (μm).

The Drude and Lorentz relation is utilized for calculating frequency dependent dielectric constant values of gold as[11]

$$\varepsilon_{\mathrm{Au}} = \varepsilon_\infty - \frac{\omega_D^2}{\omega(\omega + j\gamma_D)} - \frac{\Delta\varepsilon\,\omega^2}{(\omega^2 - \Omega_L^2) + j\Gamma_L\omega} \tag{2}$$

where symbols $\varepsilon_\infty = 5.9673$ and $\varepsilon_{\mathrm{Au}}$ are used for permittivity at high frequency and permittivity of gold. The angular frequency (ω) of the incident light is connected to the wavelength with relation $2\pi c/\lambda$, where speed of light is represented by alphabet c. The plasma and damping frequencies are $\omega_D/2\pi = 2113.6$ THz and $\gamma_D/2\pi = 15.92$ THz respectively. The spectral width of Lorentz oscillator and and oscillator strength are $\Gamma_L/2\pi = 104.86$ THz and $\Omega_L/2\pi = 650.07$ THz respectively. The weighting factor is $\Delta\varepsilon = 1.09$

The wavelength-dependent refractive index of graphene is calculated from equation (3) as[48].

$$n_g = 3 + \frac{i \times A_1 \times \lambda}{3} \tag{3}$$

where, $A_1 = 5.446\ \mu m^{-1}$ and λ is the incident wavelength.

All the simulation results of this work are obtained from softwares COMSOL Multiphysics 6.0 and MATLAB. The perfectly matched cylindrical layer (PMCL) of optimum thickness is used to prevent reflection from the structural boundaries.

The evaluation of the working (performance) of this sensor design is done on the basis of confinement loss (CL), sensitivity S(λ) and wavelength resolution R(λ).

At a particular wavelength, when real part of n_{eff} of guided mode coincides with that of the surface plasmon polariton (SPP) mode, the SPR condition is fulfilled. This phase-matching condition leads to strong coupling, causing a significant optical power transmission from core to metallic region. As a result, the CL rises considerably, and therefore its accurate evaluation is crucial. It is determined from equation (4) as[49]

$$\mathrm{CL} = \frac{40\pi}{\lambda \ln(10)} \cdot\ Im(n_{\mathrm{eff}}) \times 10^4 [dB/cm] \tag{4}$$

where $Im(n_{eff})$ is representing imaginary part ERI.

The wavelength dependent sensitivity of this sensor is calculated under wavelength interrogation method (WIM) as[47]

$$S(\lambda) = \frac{\Delta\lambda_{\mathrm{peak}}}{\Delta n_a}(nm/RIU) \tag{5}$$

where, $\Delta\lambda_{\mathrm{peak}}$ is the change in the wavelength of resonance .due to two consecutive positions of (CL) peaks due to variation in analyte RI Δn_a.

The ability of any sensor to scale minute deviation in the analyte RI is examined in terms of its wavelength resolution as defined in equation (6) below[47]

$$R(\lambda) = \Delta n_a \times \frac{\Delta\lambda_{\mathrm{min}}}{\Delta\lambda_{\mathrm{peak}}} \tag{6}$$

In equation (6) $\Delta\lambda_{\mathrm{min}}$ is the minimum spectral resolution (MSR) which has been taken to be 0.1 nm. Rest notations are similar to equation (5).

The amplitude sensitivity (S_a) of any PhCF sensor can be obtained from equation (7) as[47],

$$S_a = -\frac{1}{\alpha(\lambda, n_a)} \frac{\Delta\alpha(\lambda, n_a)}{\Delta n_a} \text{ (1/RIU)} \tag{7}$$

Here, $\alpha(\lambda, n_a)$ specifies the confinement loss value for each wavelength at fixed n_a. The Δn_a represents a small change in analyte RI value of n_a resulting measurable shift in wavelength of resonance of that of CL spectra. $\Delta\alpha(\lambda, n_a)$ is the change in CL at wavelength of resonance value due to tiny change in analyte RI Δn_a. Amplitude sensitivity is strongly dependent upon change in CL $\Delta\alpha(\lambda, n_a)$ fixed value of corresponding to Δn_a.
Also, we calculated the figure of merit (FOM), one of the important parameters in sensor performance. It is defined as the ratio of $S(\lambda)$ to FWHM, by equation (8)[50]. FWHM is the full width at half maximum of the CL spectra.

$$FOM = \frac{S(\lambda)}{FWHM} \text{ RIU}^{-1} \tag{8}$$

Analysis of the result and Discussion

In obtaining the simulation data pertaining to dual-core SPR-based PhCF biosensor design, we have used COMSOL Multiphysics 6.0 and MATLAB software. The data of the optimized structure is further used to analyze the behaviour of core-guided and SPP (surface plasmon polariton) modes corresponding to both x- and y- polarizations. The confinement loss (CL), dispersion relation and electric field distribution plots corresponding to both x and y-polarization for core-guided and SPP modes are examined first. In a dual-core PCF, the two guided modes each of distinct field profile and effective refractive index combine to form symmetric and anti-symmetric super-modes. The symmetric mode confines energy between the cores, whereas anti-symmetric mode pushes more of field energy towards the metal–graphene interface. The interaction of symmetric and anti-symmetric super-modes with the cladding boundary is purely different. Both requires a distinct phase-matching condition with the SPP mode. When the $n_eff.$ of any one of the super modes is reached to the SPP mode, strong resonance coupling occurs. This dual-pathway interaction is responsible for the increase in the overall coupling efficiency, resonance sharpness and greater wavelength sensitivity in contrast to the single-mode system.

The asymmetry in the sequence, size, or position of air holes created inside the fiber cladding is responsible for the double refraction phenomenon, referred to as birefringence. This phenomenon introduces two orthogonal x and y polarized transverse electric modes HE_x and HE_y that propagate through the fiber core at different velocities. Consequently, each mode experiences a distinct refractive index. Thus, two orthogonal polarized modes have different refractive indices. Fig. 2 illustrates the distribution electric field associated with core-guided (fundamental) and SPP modes for both HE_x and HE_y separately under resonance for analyte of RI 1.34. This polarization dependence arises from the asymmetric field distribution in the dual-core structure, which causes the y-polarized super-mode to place more energy near the metal–graphene interface, resulting in higher confinement loss and sharper resonance. We acknowledge that, for practical applications, a robust dual-core sensor should ideally exhibit polarization-independent performance. Achieving this would require structural modifications such as introducing geometrical symmetry between the two cores, reducing birefringence, or employing circular or elliptical air-hole arrangements that equalize field overlap for both polarizations. Additionally, using isotropic plasmonic coatings or carefully adjusting graphene and gold thicknesses could further balance the x- and y-polarized modal interactions. It is beyond the scope of preent work and will be considered a pathways for future design of polarization independent dual-core SPR sensors.

Figs 2(a) and 2(b) along with 2(c) and 2(d) illustrate the distribution of field of core (fundamental) and SPP modes for HE_x and HE_y at wavelengths resonance 800 nm and 850 nm, respectively, for an analyte of RI 1.34. It is evident from Figs. 2(a) and 2(c) that the electric field distributions on the surface of gold are noticeably stronger for the HE_y core mode in contrast with HE_x core mode. This enhanced field represents the evanescent component responsible for the stronger excitation of SPWs, resulting from oscillating free electrons under HE_y polarization as shown in Fig. 2(c). Additionally, this intensified evanescent field facilitating efficient energy transfer from the core mode to the SPP mode corresponding to HE_y in contrast to HE_x, as illustrated in Figs. 2(b) and 2(d). The comparison of simulated field distributions at the graphene–analyte gold–analyte interface would clearly show stronger field localization and higher plasmonic confinement in the presence of graphene, confirming that its role goes well beyond preservation and directly enhances sensing performance interface of this work with gold-analyte interface of design reported in ref. (6) clearly show that the presence of graphene with gold is responsible for stronger field localization and higher plasmonic confinement. It also confirms that the role of graphene goes well beyond preservation and directly enhances sensors performance.

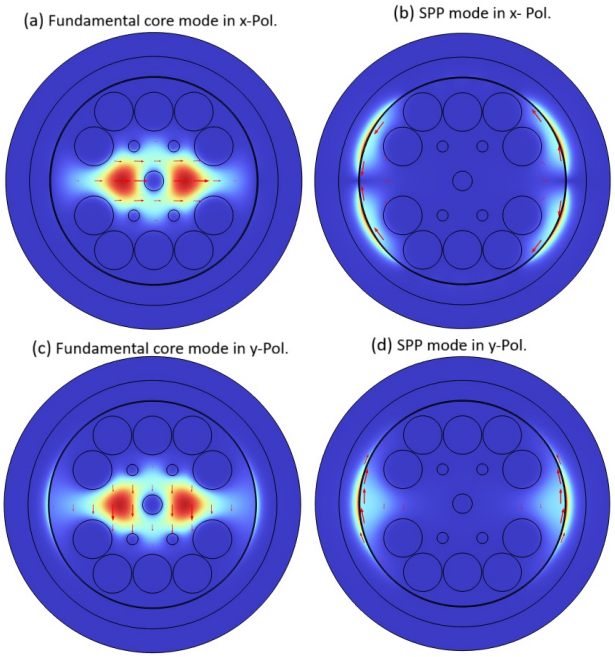

Figure 2. Electric field distribution of light propagating inside PhCF design loaded with analyte of RI 1.34. At resonant wavelength λ= 800 nm, under HE_x modes (a) fundamental and (b) SPP, at resonant wavelength λ= 850 nm, under HE_y modes (c) fundamental and (d) SPP.

Next, the variation of confinement loss and dispersion relation (giving effective refractive index variation) on wavelength, ranges from 700 nm and 1000 nm corresponding to HE_x and HE_y fundamental core modes, is illustrated in Fig. 3 below. It also includes information on effective refractive index variations of HE_x and HE_y SPP modes.

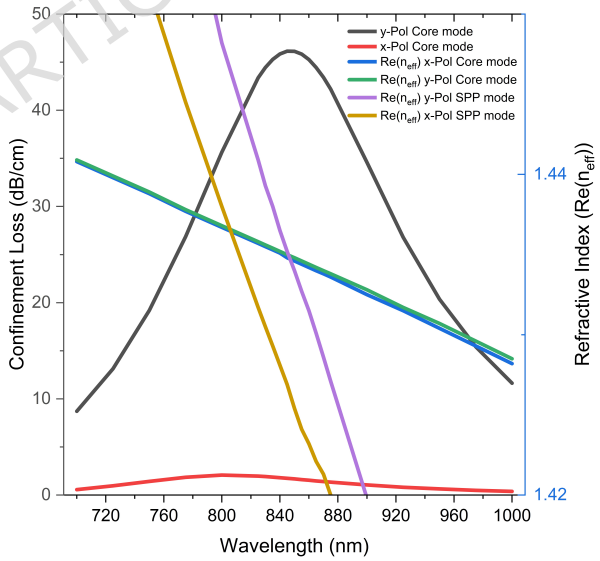

Figure 3. Depiction of confinement loss, fundamental core and SPP modes dependent on wavelength corresponding to x- and y- polarization, when the structure is loaded with analyte of RI 1.34. Blue and green color solid lines are representing real ($n_{eff.}$) value of core modes under HE_x and HE_y polarization cases, yellow and purple colour soild lines are showing real ($n_{eff.}$) value of SPP mode under HE_x and HE_y polarization cases and red and black color solid lines are indicating CL of core mode under HE_x and HE_y polarization cases.

Figure 3 illustrates the change in the real part of ERI value corresponding to HE_x and HE_y polarized core (fundamental) and SPP modes shown by solid blue, green, and purple, yellow Coloured lines respectively, when analyte of RI value of 1.34 is poured in to the sensor. The SPP mode exhibits a steeper change in the real part of ERI compared to the core (fundamental) mode. The real ($n_{eff.}$) part core (fundamental) mode intersects the SPP mode at a particular wavelengths of 800 nm and 850 nm, corresponding to HE_x and HE_y polarized modes, respectively.

These are known as points of phase matching points (PMPs) corresponding to x-and y-polarized TE modes. At phase matching points, real parts of ERI values of fundamental core mode become equal to the SPP mode. Determination of a phase matching condition is an essential requirement for any SPR based PhCF sensor because it reflects strong energy transfer from the core destination mode to SPP destination mode at PMP. This energy transfer from core cladding to dielectric metal interface is responsible for generation of surface plasmon waves(SPWs). Fig. 3 shows that our structure has the maximum confinement loss associated with the HE_x and HE_y fundamental core modes of 2.03 dB / cm and 46.1352 dB / cm, respectively. Also, it indicates that CL associated with HE_y core mode is higher than that of HE_x core mode. This higher CL is due to the stronger evanescent waves which in turn allow maximum transfer of energy from core-to SPP-mode. This is the reason for limiting this simulation work only for y-polarized fundamental core mode.

Any change in analyte RI value under investigation significantly impacts on the ERI value of the sensor dependent on the incident wavelength for both the core-and SPP-modes. Here analyte RI value changes from 1.30 to 1.39 in the steps of 0.01. This incremental increase in analyte RI value also increases the CL connected with core (fundamental) mode of the proposed sensing structure under y-polarization case because it lowers down the RI contrast of core and cladding. Moreover, this incremental change in RI also shifts the resonant wavelength of the respective CL toward the higher side of wavelength, as evident from Figure 4. The resonant wavelengths, corresponding to analyte of RIs 1.30, 1.31, 1.32, 1.33, 1.34, 1.35, 1.36, 1.37, 1.38 and 1.39 are 725 nm, 750 nm, 775 nm, 800 nm, 850 nm, 900 nm, 950 nm, 1025 nm, 1100 nm and 1400 nm respectively.

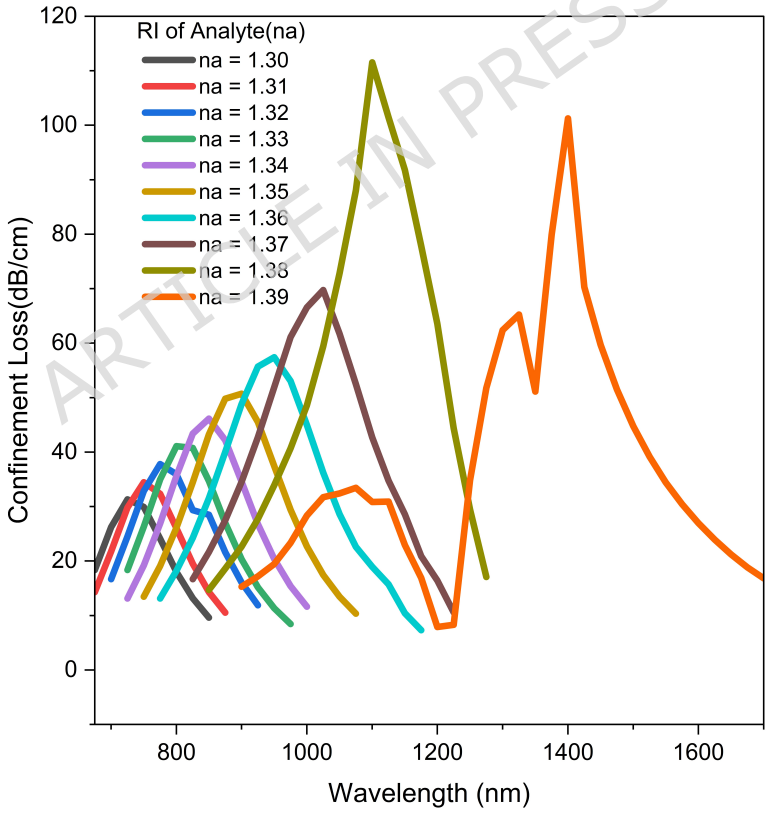

Figure 4. Wavelength-dependent confinement loss spectra of the proposed PhCF sensor corresponding to y-polarized transverse electric (HE_y) fundamental mode, evaluated separately for different analytes. The wavelength of resonance values of CL loss spectra, evaluated for analyte RI values of 1.30, 1.31, 1.32, 1.33, 1.34, 1.35, 1.36, 1.37, 1.38, and 1.39 are 725 nm, 750 nm, 775 nm, 800 nm, 850 nm, 900 nm, 950 nm, 1025 nm, 1100 nm and 1400 nm respectively.

It can be clearly seen from Fig. 4 that our design loaded with analyte's RI 1.39 shows multiple peaks in the CL plot shown

in orange colour solid line curve. This unusual behaviour at higher RIs is due to tunable behaviour of graphene coated over gold layer.

Next, the working efficiency of the biosensor proposed here, is examined by evaluating its key parameters of sensing characteristics like wavelength sensitivity, wavelength resolution, amplitude sensitivity, FOM with the help of Eqs. defined in (5), (6), (7) and (8) respectively under the light of wavelength interrogation method due to its superiority over amplitude interrogation method. The CL, wavelength sensitivity , wavelength resolution, amplitude sensitivity and amplitude resolution, FWHM, FOM along with resonant wavelength and resonant wavelength shift values corresponding to analyte RI values 1.30,1.31,1.32,1.33,1.34,1.35,1.36,1.37,1.38 and 1.39 separately loaded in to PhCF based SPR sensor are listed in Table 1 below. These numeric values are obtain by using equation (5) to (8) discussed above. For instance the change in analyte RI values from 1.39 to 1.38 results the respective dependence of wavelength of resonance of CL under HE_y polarized core mode from 1400 nm to 1100 nm as depicted in Fig. 4 yielding a maximum wavelength dependent sensitivity and resolution values of 30000 nm/RIU and 3.3×10^{-6} RIU respectively. Under this situation FOM, amplitude sensitivity and FWHM values of the design are reached to 156.25 RIU^{-1}, 765.015 RIU^{-1} and 192 nm respectively.

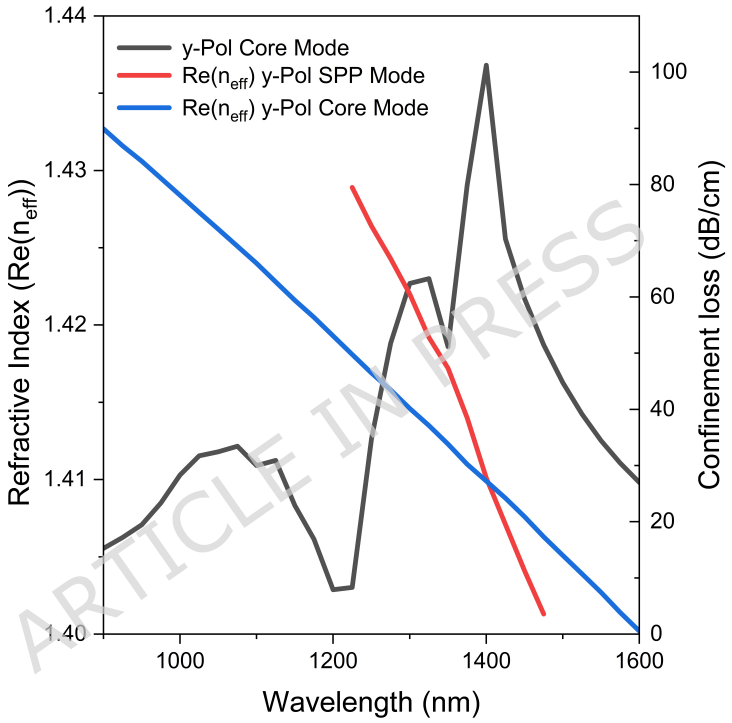

Figure 5. Wavelength dependent real part of ERIs values (left y-axis) of core and SPP modes and CL spectra of proposed PhCF (right y-axis) SPR based sensor design under HE_y polarization mode only loaded with analyte RI 1.39.

It is also obivous from figure 4 that at n_a = 1.39, the appearance of multiple resonance peaks is most likely due to coupling with different core-supported modes rather than a single SPP branch. As the analyte RI increases, the ERI values of the symmetric and anti-symmetric super-modes of the dual-core structure shift upward. Each of these modes may independently satisfy the SPP phase-matching condition. When this happens, both super-modes can couple to the plasmonic interface, producing more than one resonance peak in the confinement-loss spectrum. This behaviour indicates excitation of distinct resonance states either the fundamental SPP mode and a higher-order or hybridized SPP like mode, or separate resonances associated with the two super-modes. In our case at n_a = 1.39 in wavelength range 900 nm to 1600 nm the real part of ERI of core and SPP modes intersect at once yielding a resonant wavelength of 1400 nm corresponding to this, CL value reaches to maximum at 101.25 dB/cm as depicted in Figure 5. Though at n_a = 1.39 two peaks of different resonant wavelengths are existing in the CL spectra, wavelength of resonance 1400 nm satisfies phase matching requirements as evident from Fig. 5. This behaviour can also be verified by analyzing mode profile at each resonant wavelength as $\lambda_1 = 1325nm$, $\lambda_2 = 1400nm$ depicted in Fig. 6 and 7 respectively. Both the field plots indicate whether each peak is produced by a different coupling interaction between the symmetric or anti-symmetric super- and SPP-mode modes. Fig. 6(a) shows symmetric mode coupling mechanism responsible for field localization between two cores, whereas Fig. 6(b) indicates that field is pushed towards the plasmonic interface due to

antisymmetric mode coupling.

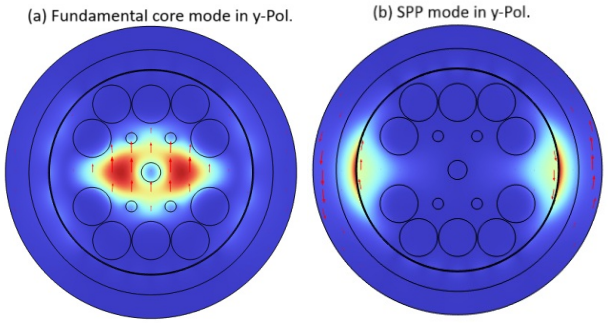

Figure 6. Electric field distribution of light propagating inside PhCF design loaded with analyte of RI 1.39. At wavelength λ= 1325 nm, (a) fundamental core and (b) SPP modes have real part of ERIs of 1.4136 and 1.4286 respectively.

On other hand figure 7 depicts core mode profile corresponding core and SPP modes to phase matching condition arries at resonant wavelength 1400 nm corresponding to y-polarized HE_y mode. This analysis clears that each resonance has a clear physical origin, ensuring that the peaks are not due to numerical anomalies but due to super mode-SPP coupling events.

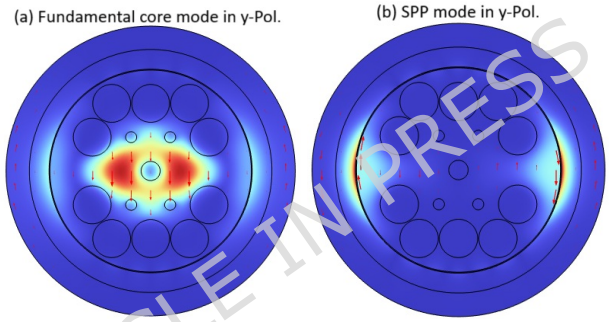

Figure 7. Electric field distribution of light propagating inside PhCF design loaded with analyte of RI 1.39. At resonant wavelength λ= 1400 nm, (a) fundamental core and (b) SPP modes both have same real part of effective refractive index values of 1.4099.

Table 1. Performance summarization of the bio-sensor loaded separately with analytes of RIs 1.30 to 1.39.

Analyte RI (n_a)	**Resonant wavelength** λ_{peak} **(nm)**	λ_{peak} **difference** $\Delta\lambda_{peak}$ **(nm)**	**CL**(λ) **(dB/cm)**	**S**(λ) **(nm/RIU)**	**R**(λ) **(RIU)**	**FWHM (nm)**	**FOM** (RIU^{-1})	**Amplitude Sensitivity** (RIU^{-1})
1.30	725	25	31.30698033	2500	4.00×10^{-5}	135	18.51852	48.8714
1.31	750	25	34.46721206	2500	4.00×10^{-5}	151	16.55629	85.663
1.32	775	25	37.80946213	2500	4.00×10^{-5}	181	13.81250	27.8975
1.33	800	50	41.09972722	5000	2.00×10^{-5}	173	28.90173	82.4248
1.34	850	50	46.13523455	5000	2.00×10^{-5}	177	28.24859	95.0712
1.35	900	50	50.70765845	5000	2.00×10^{-5}	190	26.31579	118.193
1.36	950	75	57.41784209	7500	1.33×10^{-5}	200	37.50000	174.419
1.37	1025	75	67.76460133	7500	1.33×10^{-5}	221	33.93665	510.507
1.38	1100	300	111.5630118	30000	3.33×10^{-6}	192	156.25	765.015
1.39	1400	NA	101.2538416	NA	NA	120	NA	NA

Resonant wavelength behaviour of amplitude dependent sensitivity of this bio sensing design separately loaded with analyte RIs of 1.30,1.31,1.32,1.33,1.34,1.35,1.36,1.37,1.38 and 1.39 based on amplitude interrogation as depicted in Fig.8 below.

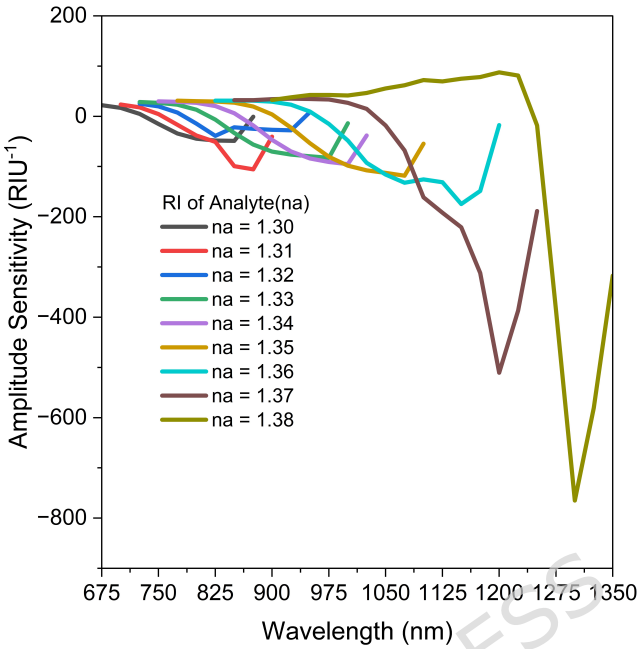

Figure 8. Depiction of wavelength dependent amplitude sensitivity of proposed design separately loaded with analytes of RI variation from 1.30 to 1.39 in steps of 0.01.

The results witness that any incremental increase in analyte RI from 1.30 to 1.39 in steps of 0.01, the amplitude sensitivity correspondingly increases from a minimum of $48.3714 RIU^{-1}$ to maximum of $765.015 RIU^{-1}$. The nature of this variation is red shift. The estimated value of amplitude resolution of our design is 1.30×10^{-5} RIU corresponding to highest amplitude based sensitivity value of 765.015 RIU^{-1} and transmission detection precision of 1% for sample of RI 1.39. The major drawback of amplitude sensitivity is its dependency upon intensity measurements of the reflected light from plasmonic metallic layer. It is also dependent on RI of analyte. The amplitude sensitivity measurements requires a fixed wavelength light source without any need of spectral analysis. This technique does not consider any vulnerable changes of light fluctuations as well as absorption of light by the surroundings. On the other hand sensitivity calculation of any PhCF-SPR biosensor design based on wavelength interrogation are widely preferred due to its excellent spectral response over a given range of wavelength. It also enhances the order of resolution as compared to amplitude interrogation methods (AIM) based sensitivity calculation. Despite the above narrated advantage of wavelength sensitivity based on wavelength interrogation method (WIM) exhibiting better detection response in the sensing of bio analytes, as compared to amplitude sensitivity based on amplitude interrogation method. Next, we have investigated the dependency of analyte RI on FWHM of respective CL spectra including FOM values of design. Fig. 9 illustrates the dependence of FWHM and FOM values on RIs of different analyte.

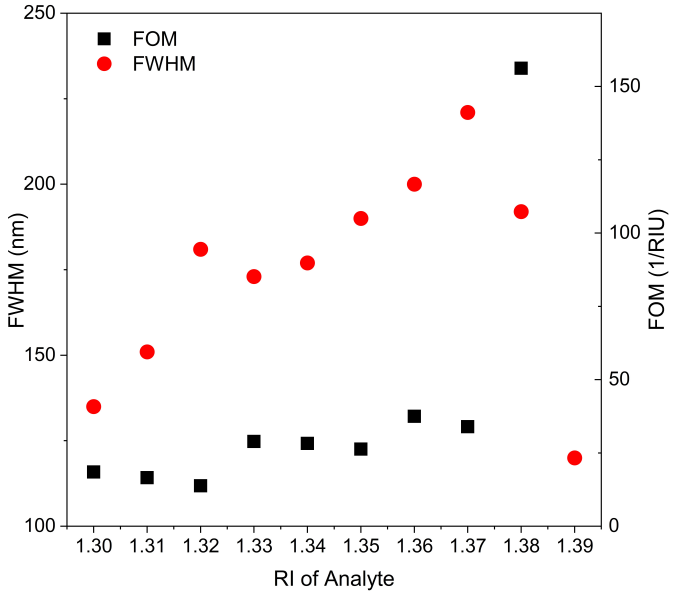

Figure 9. Dependence of FWHM value of CL spectra shown in Fig. 4 and FOM values shown in left and right y-axis respectively on RI values of analytes varies from 1.30 to 1.39 as steps of 0.01.

It shows in response to the RI variations of analytes from 1.30 to 1.39 in steps 0.01. FOM values varies from maximum of 156.25 RIU^{-1} to minimum of 13.81250 RIU^{-1}. Under this variation of RI, FWHM values are varied from maximum of 221 nm to minimum of 120 nm. Data summarized in the plotting of Fig. 8 and 9.

Further we have examined the role of thickness of graphene and gold on the biosensor performance qualitatively. In any PhCF sensing design optimization of the thickness of plasmonic layer along with addition layer if any is one of the mandatory requirements. In the following subsections we have made an attempt to elaborate the process of optimization of thickness of graphene and gold layers of the sensing design.

Role of Graphene and Gold Layer Thicknesses in Determining Sensor Performance

This section highlights the very important aspect of selecting an appropriate thickness of Graphene (t_{gr}) and Gold (t_{gold}) layers on the performance of our design. First, the significant impact of the Graphene material and it's thickness on the performance of the design is being discussed. The purpose of using a thin graphene layer over the gold film is to significantly enhance the sensing performance due to the association of the plasmonic properties of gold with the unique characteristics of graphene. Graphene offers a large surface-to-volume ratio and strong biomolecule adsorption capability, which improves the interaction between analyte and sensing interface. It also strengthens light–matter interaction and sharpens plasmon resonance by reducing damping losses typically associated with gold. Moreover, graphene protects the gold layer from oxidation, enhances chemical stability, and provides tunable optical properties through Fermi level adjustment. These features collectively lead to higher sensitivity, better resonance quality, and longer sensor durability compared to gold alone.

Besides this the role of the graphene is to enhance the plasmonic response with the help of wavelength-dependent surface conductivity of the graphene. It results in the modification of the SPP dispersion responsible for confinement of an electric-field at the metal–analyte boundary, yielding as strong field localization which initiates a pronounced shift in the wavelength of resonance due to any tiny change in analyte RI. The thin architecture of the PhCF sensor also triggers an additional charge oscillation, for the reinforcement of the plasmon excitation yielding the narrow resonance linewidth. Additionally, the optical properties of the gold are preserved due to chemically stable barrier formed by graphene. The application of graphene layer in to the structure is to improve the active field and stability of the system for protection of gold coating.

The two closely spaced cores of a dual core PhCF design generate super-modes strongly aligned toward the plasmonic layer of the structure in contrast to single-core mode for efficient interaction between super-modes and SPP mode. This interaction eases the selection of phase matching point highly responsive to even tiny change in RI value of bio-analyte. It also allows the more optical energy transfer into the plasmonic mode at resonance. Finally, this dual-mode interaction substantially enhances the strength of resonance governing overall WS value of the sensor. The dual-core fiber sensors create sharper and stronger resonance peaks in addition to larger wavelength shifts, whereas a single guided mode due to weaker interaction is observed in single-core design resulting in the reduction in the coupling strength.

Fig.10 depicts the change in the CL spectra of the proposed design at fixed $t_{gold} = 40nm$ and two different graphene layer thicknesses $t_{gr} = 9.18$ nm and 9.86 nm, loaded separately this two analytes of RIs 1.38 and 1.39. It is seen from Fig. 10 that proposed sensor ($t_{gr} = 9.86$ nm and $t_{gold} = 40$ nm) loaded with analyte of RI 1.38 possesses a resonant peak centered at wavelength 1150 nm as shown by black colour solid line curve. This resonant peak acquires new position of center wavelength 1400 nm when the structure is loaded with another analyte of RI 1.39 as shown by red colour solid line curve. Under these conditions, the sensor's WS increases to 25,000 nm/RIU. On the other hand, the structure with $t_{gr} = 9.18$ nm and $t_{gold} = 40$ nm exhibits a minimum wavelength sensitivity of 20,000 nm/RIU for analyte RIs of 1.38 and 1.39, as shown in Fig. 10. Therefore, any decrease or increase in t_{gr} from 9.52 nm to 9.18 nm or from 9.52 nm to 9.86 nm —substantially weakens the WS value of the optimized design from 30,000 nm/RIU to 25,000 nm/RIU or 20,000 nm/RIU, respectively.

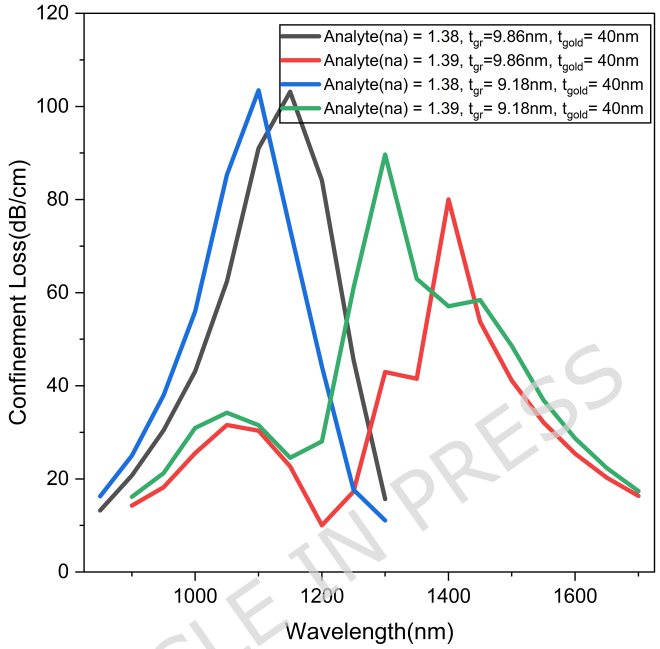

Figure 10. Wavelength-dependent confinement loss spectra of proposed PhCF sensing designs (i) $t_{gr} = 9.18$ nm and $t_{gold} = 40$ nm and (ii) $t_{gr} = 9.86$ nm and $t_{gold} = 40$ nm. The CL curves of HE_y polarized fundamental core mode of first design loaded separately with analyte of refractive indices 1.38 and 1.39 are shown in colours blue and green respectively whereas for second design the respective CL spectra are shown in colours black and red, respectively. The resonant wavelengths of confinement loss spectra shown in colours blue, black, green and red are 1100 nm, 1150 nm, 1300 nm and 1400 nm, respectively.

This is because the structure shifts the wavelength of resonant from 1100 nm to 1300 nm corresponding to RI change in the analyte from 1.38 to 1.39, respectively. It is shown by the solid blue and green line curves of Fig. 10. Thus, it confirms that the optimal graphene layer thickness of our design is 9.52 nm, consistent with the findings presented earlier in the discussion of Fig. 4. All the graphene layer thicknesses are taken in the integer multiples of a graphene monolayer thickness 0.34 nm. It yields the integer multiples of 29, 28 and 27 corresponding to graphene layer of thicknesses 9.18 nm, 9.52 nm and 9.86 nm respectively.

After discussing the optimization of graphene layer thickness of the proposed SPR based PhCF sesnor to 9.52 nm, we have given our efforts to optimize the gold layer thickness (t_{gold}) of the design due to it's very important sensing role in sensor's performance. For the fulfillment of the purpose, the sensitivities of the three different SPR-based PhCF designs of different gold layer thicknesses with identical graphene layer thickness as (i) $t_{gr} = 9.52$ nm and $t_{gold} = 35$ nm, (ii) $t_{gr} = 9.52$ nm and $t_{gold} = 40$ nm, and (iii) $t_{gr} = 9.52$ nm and $t_{gold} = 45$ nm, each under the guidance of analytes of RIs ranging from 1.38 and 1.39 separately have been examined. In order to find most sensitivity design amongst the above three, we have investigated wavelength-dependent confinement loss of each structure separately loaded with analyte of refractive indices 1.38 and 1.39 as depicted in Fig. 11 below. The CL curves under HE_y polarized fundamental core mode of design having $t_{gr} = 9.52$ nm and $t_{gold} = 35$ nm loaded separately with analyte of refractive indices 1.38 and 1.39 are shown in colours blue and green, respectively whereas the design having $t_{gr} = 9.52$ nm and $t_{gold} = 45$ nm possesses the CL spectra shown in colors black and red representing analytes of RI 1.38 and 1.39 respectively. The resonant wavelengths associated with confinement loss spectra shown in colours blue, black, green and red are 1100 nm, 1150 nm, 1350 nm and 1350 nm, respectively as evident from Fig. 11. This process yields the most appropriate gold layer thickness of the structure to 40 nm. Thus, the structure with $t_{gr} = 9.52$ nm

and $t_{gold} = 40$ nm is considered to be an optimized structure yielding its highest WS value of 30000 nm/RIU and lowest limit of resolution value of 3.33×10^{-6} RIU.

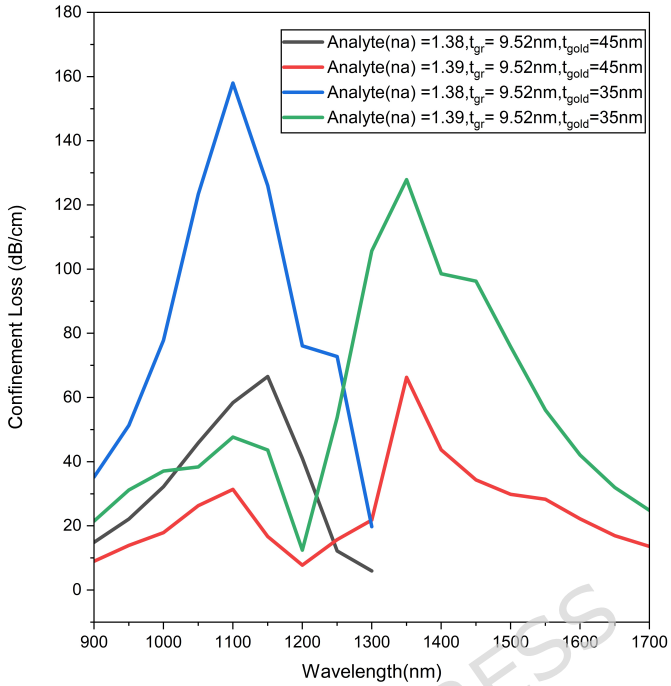

Figure 11. Wavelength-dependent confinement loss spectra of proposed PhCF sensing designs having (i) $t_{gr} = 9.52$ nm and $t_{gold} = 35$ nm and (ii) $t_{gr} = 9.52$ nm and $t_{gold} = 45$ nm. The CL curves under HE_y polarized fundamental core mode of first design loaded separately with analyte of refractive indices 1.38 and 1.39 are shown in colours blue and green, respectively whereas for second design the respective CL spectra are shown in colours black and red, respectively. The resonant wavelengths of confinement loss spectra shown in colours blue, black, green and red are 1100 nm, 1150 nm, 1350 nm and 1350 nm, respectively.

Role of Analyte RI Changes on Resonant Wavelength and Confinement Loss

Here, we investigated the effect of analyte RI alterations on the wavelength of resonance and the peak value of CL responsible for the minute sensing and detection qualites of the design. For this purpose, the dual y axis plot having common x axis is used. The left and right y axes of Fig. 12 show variations of the resonant wavelengths and the maximum value of confinement loss, respectively, with a common x axis containing the discrete values of refractive indices of analytes ranging from 1.30–1.39. The highest CL value associated with HE_y polarized core mode increases in concordance with the increase in the value of analyte of RI values of analyte because it reduces the RI contrast between core and cladding. Moreover, the resonant wavelength starts to move higher wavelength side as analyte RI changes from 1.30 to 1.39. The wavelengths of resonance reach to 725 nm, 750 nm, 775 nm, 800 nm, 850 nm, 900 nm, 950 nm, 1025 nm, 1100 nm, and 1400 nm corresponding to analyte's refractive index 1.30, 1.31, 1.32, 1.33, 1.34, 1.35, 1.36, 1.37, 1.38 and 1.39 respectively, as depicted in Figure 12. The variations of resonant wavelengths and the maximum value of confinement loss of the optimized design dependent on different refractive indices are shown by blue colour soild dots and red colour solid squares respectively in Figure 12. The fourth-order polynomial fitting shown in red dashed line is applied to the resonant wavelength data. This fitting utilizes the analyte RI as independent variable and wavelength of resonance as dependent variable. It yields R^2 equal to 0.99200 which indicates a very reasonable fitting between the simulated data and the curve fitting model. Here, R is the statistical software language. It measures how perfectly the regression model describes the dependence of the dependent variable on the independent variable.

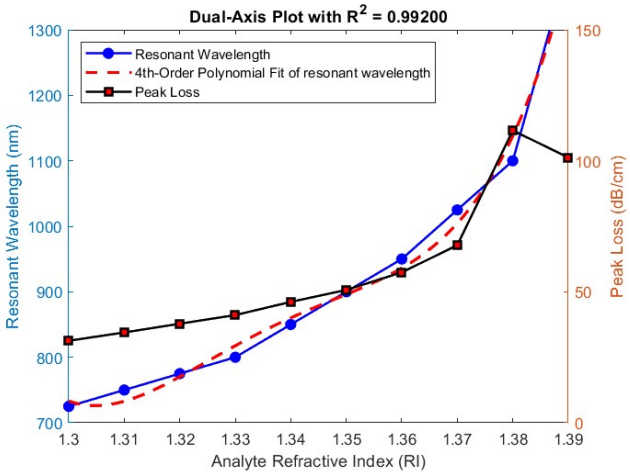

Figure 12. The dual y-axis plot having common x axis is used. The left and right y axes show variations of the resonant wavelengths and the maximum value of confinement loss, respectively, with a common x axis containing the discrete values of RIs of analytes in the ranging from 1.33–1.39. The variations of resonant wavelengths and the maximum value of confinement loss of the optimized design dependent on different RIs depicted by by solid blue colored dots and solid red Coloured squares respectively. The fourth-order polynomial fitting shown in red dashed line is applied to the resonant wavelength data.

Finally, the comparison of the proposed SPR based PhCF sensor with related sensing works conducted by different research groups is presented. The group of Rifat et al. studied a practical approach of bio sensing design consisted of SPR-PhCF. This chemically stable design utilizes gold layer deposited on extremely outer surface of the structure to ease the fabrication process. This design achieves maximum senstivity of 4000 nm/RIU[26]. Hasan et al suggested a dual-polarized SPR biosensor consisted of PhCF whose outer layer is made up of gold to facilitate the fabrication. This design loaded with analyte of refractive index 1.37 achieves highest WS value of 4600 nm/RIU and 4300 nm/RIU under HE_x and HE_y polarized modes respectively[20]. Later, Rifat et al. (2016) introduced a graphene coated copper-based SPR PhCF biosensor. They have used graphene coating over plasmonic metal copper to prevent it from oxidation. They have found an enhanced WS of 2000 nm/RIU for analytes of RI rangeing from 1.33 to 1.37[12]. In another work, Hasan et al in 2018 demonstrated a niobium nanofilm–based PhCF sensor with an additional Al_2O_3 layer, offering the maximum declared sensitivities of wavelength and amplitude to 8000 nm/RIU and 1560 per RIU respectively, attributing to strong field confinement and tunable resonance behavior[31]. Ahmed et al. (2019) suggested a dual-core hexagonal PhCF design consisted of externally deposited plasmonic layer of gold, allowing strong mode coupling between the two cores and the plasmonic gold layer, resulted an exceptionally high sensitivities of wavelength and amplitude to 16,000 nm/RIU and 2255 per RIU, respectively along with considerably higher resolution value of 6.25×10^{-6} RIU[6]. In contrast, D-shaped photonic biosensor consisted of 20 nm wide gold coating over the polished surface reported by An et al. (2017) achieved a WS of 10493 nm/RIU in addition to resolution of 9.53×10^{-6} RIU[30]. Although this design demonstrates strong plasmonic interaction, it faces several fabrication challenges arising from the need for highly precise polishing.

Overall, while most of the above designs utilized gold as the plasmonic material, all have used finite-element modeling for obtaining simulation results. The spiral structure focuses on polarization-based enhancement, the hexagonal dual-core design achieves the highest sensitivity through dual-core coupling, whereas the D-shaped configuration possesses compactness which is necessary for strong surface interaction results suitable for biochemical sensing. In light of the data presented summarized in Table 2, It may be concluded that the proposed graphene-coated, gold-based SPR–PhCF design attains a WS of 30,000 nm/RIU, representing the highest performance among all compared configurations. Additionally it is capable of addressing large range of analytes having RIs from 1.30 to 1.39. The wavelength resolution of the proposed structure is 3.33×10^{-6} which is very low in contrast to the data presented in Table 2.

Table 2. Performance evaluation table.

Reference	Sensor design	RI detection Range	$S(\lambda)$ (nm/RIU)	Wavelength Resolution $R(\lambda)$ (RIU)	Amplitude Sensitivity (RIU^{-1})	Amplitude Resolution (RIU)
[12]	Graphene layer on Cu	1.33–1.37	2000	5×10^{-5}	140	7.1×10^{-5}
[26]	Gold-Coated	1.33–1.37	4000	2.5×10^{-5}	320	3.13×10^{-5}
[30]	D-Shaped Gold-Coated	1.33–1.38	10493	9.53×10^{-6}	N/A	N/A
[31]	Nibium and Al_2O_3	1.36–1.40	8000	1.25×10^{-5}	1560	8.64×10^{-5}
[20]	Gold-Coated Spiral PhCF	1.33–1.38	4300	2.17×10^{-5}	420.4	4.1×10^{-5}
[6]	Gold Coated dual core PhCF	1.33–1.40	16000	6.25×10^{-6}	2255	4.4×10^{-6}
This Work	**Graphene coated Gold**	**1.30-1.39**	**30000**	$\mathbf{3.33\times10^{-6}}$	**765**	$\mathbf{1.30\times10^{-5}}$

Though the resolution of this research work based on WIM is slightly less than the design reported in ref (6), the highest wavelength sensitivity of 30000 nm/RIU makes our modified design most efficient. Moreover amplitude sensitivity and corresponding resolution values of the design reported in ref (6) one higher, this calculation based on amplitude interrogation methods which are less preferred over wavelength sensitivity and wavelength resolution calculations based on wavelength interrogation methods. All the findings are obtained from numerical simulations without having any experimental realization. The overall performance of the proposed design is based on the precise measurement of the thickness of graphene along with gold layers, may create difficulties during fabrication. The strong polarization dependence yielding resonance only for y-polarized mode restricts its operation in polarization independent situation. The occurrence of multiple peaks may introduce the difficulties associated their identification for the analytes of higher analyte indices. The proposed sensor can sense the bio analytes of RIs ranging from 1.30 to 1.39 which limits its applicability of biological or chemical samples of higher refractive-indices. Furthermore, this work dose not account for any kind of tolerance related to fabrication, environmental instabilities, or real-material defectiveness. These may affect the performance predicted in simulations.

Conclusion

In conclusion, the proposed dual-core PhCF sensor composed of graphene coated gold layer is capable of accurate sensing of large range of analytes of RI change from 1.30 to 1.39. It features our design highly usable for applications of biomedical and disease diagnostics. The operating principal of proposed device is SPR. The hybrid coatings of graphene and gold improves the light-matter interaction which in turn significantly enhances the stability and the wavelength sensitivity of the design. The structure with optimized thickness of gold and graphene layers 40 nm and 9.52 nm respectively, achieves highest WS of 30,000 nm/RIU with an exceptionally low resolution of 3.33×10^{-6} RIU as expected. These results also confirm that integration of graphene with a plasmonic gold material layer in the proposed SPR-based PhCF sensor design substantially enhances the performance. The proposed work offers a promising pathway for developing next-generation bio- sensing technologies useful in precise and rapid disease detection and diagnosis for immediate care.

Data availability

The datasets of this research work will be provided by corresponding author (S.K.A.) on request to the concern.

References

1. Malek, C., Al-Dossari, M., Awasthi, S. & Aly, A. H. High performance biosensor for detection of the normal and cancerous liver tissues based on 1d photonic band gap material structures. *Sens. Imaging* **24**, 27 (2023).
2. Fakhruldeen, H. F., Zahid, A. Z., Jaafar, R. M. & Abdulkareem, A. An overview of photonic crystal fiber (pcf). *Indian J. Nat. Sci.* **9**, 0976–0997 (2019).
3. Knight, J., Birks, T., Russell, P. S. J. & Atkin, D. All-silica single-mode optical fiber with photonic crystal cladding. *Opt. letters* **21**, 1547–1549 (1996).
4. Shah, A. K. & Kumar, R. A review on photonic crystal fibers. In *International Conference on Intelligent Computing and Smart Communication 2019: Proceedings of ICSC 2019*, 1241–1249 (Springer, 2019).
5. Shukla, N., Chetri, P., Boruah, R., Gogoi, A. & Ahmed, G. A. Surface plasmon resonance biosensors based on kretschmann configuration: basic instrumentation and applications. In *Recent Advances in Plasmonic Probes: Theory and Practice*, 191–222 (Springer, 2022).
6. Ahmed, T., Paul, A. K., Anower, M. S. & Razzak, S. A. Surface plasmon resonance biosensor based on hexagonal lattice dual-core photonic crystal fiber. *Appl. optics* **58**, 8416–8422 (2019).
7. Jorgenson, R. C. & Yee, S. S. A fiber-optic chemical sensor based on surface plasmon resonance. *Sensors Actuators B: Chem.* **12**, 213–220 (1993).
8. Ahmmed, R., Ahmed, R. & Razzak, S. A. Design of large negative dispersion and modal analysis for hexagonal, square, fcc and bcc photonic crystal fibers. In *2013 international conference on informatics, Electronics and vision (ICIEV)*, 1–6 (IEEE, 2013).
9. Aoni, R. A., Ahmed, R. & Razzak, S. A. Design and simulation of duel-concentric-core photonic crystal fiber for dispersion compensation. In *CIOMP-OSA summer session on optical engineering, Design and manufacturing*, Tu2 (Optica Publishing Group, 2013).
10. Rifat, A. A., Mahdiraji, G. A., Shee, Y., Shawon, M. J. & Adikan, F. M. A novel photonic crystal fiber biosensor using surface plasmon resonance. *Procedia engineering* **140**, 1–7 (2016).
11. Sakib, M. N. *et al.* High performance dual core d-shape pcf-spr sensor modeling employing gold coat. *Results Phys.* **15**, 102788 (2019).
12. Rifat, A. A. *et al.* Copper-graphene-based photonic crystal fiber plasmonic biosensor. *IEEE Photonics J.* **8**, 1–8 (2015).
13. Dash, J. N. & Jha, R. Graphene-based birefringent photonic crystal fiber sensor using surface plasmon resonance. *IEEE Photonics Technol. Lett.* **26**, 1092–1095 (2014).
14. Saini, S. K., Maurya, V. C., Khatri, N. & Awasthi, S. K. Tamm-fano resonance based glucose sensor consisted of al and distributed bragg reflector in the visible regime. *Opt. Quantum Electron.* **57**, 655 (2025).
15. Ahmed, A. M. & Mehaney, A. Ultra-high sensitive 1d porous silicon photonic crystal sensor based on the coupling of tamm/fano resonances in the mid-infrared region. *Sci. reports* **9**, 6973 (2019).
16. Wieduwilt, T. *et al.* Ultrathin niobium nanofilms on fiber optical tapers–a new route towards low-loss hybrid plasmonic modes. *Sci. reports* **5**, 17060 (2015).
17. Ordal, M. A., Bell, R. J., Alexander Jr, R., Long, L. L. & Querry, M. R. Optical properties of fourteen metals in the infrared and far infrared: Al, co, cu, au, fe, pb, mo, ni, pd, pt, ag, ti, v, and w. *Appl. optics* **24**, 4493–4499 (1985).
18. Otupiri, R. *et al.* A novel birefrigent photonic crystal fiber surface plasmon resonance biosensor. *IEEE Photonics J.* **6**, 1–11 (2014).
19. Gao, D., Guan, C., Wen, Y., Zhong, X. & Yuan, L. Multi-hole fiber based surface plasmon resonance sensor operated at near-infrared wavelengths. *Opt. Commun.* **313**, 94–98 (2014).
20. Hasan, M. R. *et al.* Spiral photonic crystal fiber-based dual-polarized surface plasmon resonance biosensor. *IEEE Sensors J.* **18**, 133–140 (2017).
21. Peng, L. *et al.* A surface plasmon biosensor based on a d-shaped microstructured optical fiber with rectangular lattice. *IEEE photonics journal* **7**, 1–9 (2017).
22. Dash, J. N. & Jha, R. Spr biosensor based on polymer pcf coated with conducting metal oxide. *IEEE Photonics Technol. Lett.* **26**, 595–598, DOI: 10.1109/LPT.2014.2301153 (2014).

23. Luan, N., Wang, R., Lv, W. & Yao, J. Surface plasmon resonance sensor based on d-shaped microstructured optical fiber with hollow core. *Opt. express* **23**, 8576–8582 (2015).

24. Yang, X., Lu, Y., Liu, B. & Yao, J. Analysis of graphene-based photonic crystal fiber sensor using birefringence and surface plasmon resonance. *Plasmonics* **12**, 489–496 (2017).

25. Zhang, Q. *et al.* A d-type dual side-polished, highly sensitive, plasma refractive index sensor based on photonic crystal fiber. *Front. Phys.* **10**, 1008784 (2022).

26. Rifat, A. *et al.* Surface plasmon resonance photonic crystal fiber biosensor: a practical sensing approach. *IEEE Photonics Technol. Lett.* **27**, 1628–1631 (2015).

27. Hasan, M. R., Akter, S., Rifat, A. A., Rana, S. & Ali, S. A highly sensitive gold-coated photonic crystal fiber biosensor based on surface plasmon resonance. In *Photonics*, vol. 4, 18 (MDPI, 2017).

28. Yang, X., Lu, Y., Wang, M. & Yao, J. An exposed-core grapefruit fibers based surface plasmon resonance sensor. *Sensors* **15**, 17106–17114 (2015).

29. Popescu, V., Puscas, N. & Perrone, G. Power absorption efficiency of a new microstructured plasmon optical fiber. *J. Opt. Soc. Am. B* **29**, 3039–3046 (2012).

30. An, G., Hao, X., Li, S., Yan, X. & Zhang, X. D-shaped photonic crystal fiber refractive index sensor based on surface plasmon resonance. *Appl. optics* **56**, 6988–6992 (2017).

31. Hasan, M. R., Akter, S., Ahmed, K. & Abbott, D. Plasmonic refractive index sensor employing niobium nanofilm on photonic crystal fiber. *IEEE Photonics Technol. Lett.* **30**, 315–318 (2017).

32. Roggan, A., Friebel, M., Dörschel, K., Hahn, A. & Mueller, G. J. Optical properties of circulating human blood in the wavelength range 400-2500 nm. *J. biomedical optics* **4**, 36–46 (1999).

33. Walsh, M. J. & Bhargava, R. Infrared spectroscopic imaging: an integrative approach to pathology (2010).

34. Saini, S. K. & Awasthi, S. K. Sensing and detection capabilities of one-dimensional defective photonic crystal suitable for malaria infection diagnosis from preliminary to advanced stage: theoretical study. *Crystals* **13**, 128 (2023).

35. Maharana, P. K. & Jha, R. Chalcogenide prism and graphene multilayer based surface plasmon resonance affinity biosensor for high performance. *Sensors Actuators B: Chem.* **169**, 161–166 (2012).

36. Maharana, P. K., Srivastava, T. & Jha, R. Ultrasensitive plasmonic imaging sensor based on graphene and silicon. *IEEE Photonics Technol. Lett.* **25**, 122–125 (2012).

37. Wu, L., Chu, H.-S., Koh, W. S. & Li, E.-P. Highly sensitive graphene biosensors based on surface plasmon resonance. *Opt. express* **18**, 14395–14400 (2010).

38. Chou Chao, C.-T. *et al.* A simple structure of high sensitivity of plasmonic photonic crystal fiber sensors with minimal air hole density in fiber cladding. *Plasmonics* **20**, 971–982 (2025).

39. Chao, C.-T. C., Kooh, M. R. R., Chau, Y.-F. C. & Thotagamuge, R. Susceptible plasmonic photonic crystal fiber sensor with elliptical air holes and external-flat gold-coated surface. In *Photonics*, vol. 9(12), 916 (MDPI, 2022).

40. Sabaruddin, N. R., Tan, Y. M., Chou Chao, C.-T., Kooh, M. R. R. & Chou Chau, Y.-F. High sensitivity of metasurface-based five-band terahertz absorber. *Plasmonics* **19**, 481–493 (2024).

41. Chou Chau, Y.-F. Multiple-mode bowtie cavities for refractive index and glucose sensors working in visible and near-infrared wavelength ranges. *Plasmonics* **16**, 1633–1644 (2021).

42. Chau, Y.-F. C. Enhanced plasmonic waveguide sensing performance with a semicircular-ring resonator. *Micro Nanostructures* **174**, 207469 (2023).

43. Chau, Y.-F. C. Enhancing imaging capabilities with a high-sensitivity multichannel optical filter. *Micro Nanostructures* **186**, 207732 (2024).

44. Chao, C.-T. C. *et al.* Improving temperature-sensing performance of photonic crystal fiber via external metal-coated trapezoidal-shaped surface. *Crystals* **13**, 813 (2023).

45. Chou Chao, C.-T. & Chou Chau, Y.-F. Highly sensitive multichannel fano resonance-based plasmonic sensor for refractive index and temperature sensing application. In *Photonics*, vol. 10(1), 82 (MDPI, 2023).

46. Sorathiya, V., Lavadiya, S., Faragallah, O. S., Eid, M. M. & Rashed, A. N. Z. D shaped dual core photonics crystal based refractive index sensor using graphene–titanium–silver materials for infrared frequency spectrum. *Opt. Quantum Electron.* **54**, 290 (2022).

47. Meng, X. *et al.* Analysis of double peak detection in a d-shaped photonic crystal fiber plasmonic sensor. *Plasmonics* **16**, 761–768 (2021).

48. Li, T., Zhu, L., Yang, X., Lou, X. & Yu, L. A refractive index sensor based on h-shaped photonic crystal fibers coated with ag-graphene layers. *Sensors* **20**, 741 (2020).

49. Kalyoncu, C., Yasli, A. & Ademgil, H. Machine learning methods for estimating bent photonic crystal fiber based spr sensor properties. *Heliyon* **8** (2022).

50. Chen, L.-Q., Wu, Y.-C., Liu, Y., Cai, H. Y. & Liu, J. Highly sensitive dual-function sensor for refractive index and temperature using d-shaped microchannel photonic crystal fiber. *Opt. Express* **32**, 12405–12418 (2024).

Acknowledgments

The authors extend their appreciation to the Deanship of Research and Graduate Studies at King Khalid University for funding this work through Large Research Project under grant number RGP2/237/46.

Author contributions

The main idea was conceptualize by S.K.A., V.C.M., and Y. T. after detailed discussion. The necessary simulation requirements was fulfilled by V.C.M and A.D.V under the guidance of S.K.A.. The first draft of the work was shaped by V.C.M. and Y.T.. The result analysis was carried out by V.C.M. and A.D.V. under supervision of S.K.A.. The editing, revision and initial review were handled by V.C.M.. Finally all authors have contributed to the manuscript.

Funding

The funding pertaining to this work was supported under Deanship of Research and Graduate Studies from Large Research project at King Khalid University under grant number RGP2/237/46.

Declarations

Competing interests

It is declare that authors have no conflict of interest.

Additional information

Correspondence author S.K.A. will be requested for datasets of this work.